



**HAL**  
open science

# Multiple nitrogen reservoirs in a protoplanetary disk at the epoch of comet and giant planet formation

Pierre Hily-Blant, V Magalhaes de Souza, J Kastner, T. Forveille

► **To cite this version:**

Pierre Hily-Blant, V Magalhaes de Souza, J Kastner, T. Forveille. Multiple nitrogen reservoirs in a protoplanetary disk at the epoch of comet and giant planet formation. *Astronomy and Astrophysics* - A&A, In press. hal-02330688v1

**HAL Id: hal-02330688**

**<https://hal.science/hal-02330688v1>**

Submitted on 24 Oct 2019 (v1), last revised 15 Nov 2019 (v2)

**HAL** is a multi-disciplinary open access archive for the deposit and dissemination of scientific research documents, whether they are published or not. The documents may come from teaching and research institutions in France or abroad, or from public or private research centers.

L'archive ouverte pluridisciplinaire **HAL**, est destinée au dépôt et à la diffusion de documents scientifiques de niveau recherche, publiés ou non, émanant des établissements d'enseignement et de recherche français ou étrangers, des laboratoires publics ou privés.

LETTER TO THE EDITOR

# Multiple nitrogen reservoirs in a protoplanetary disk at the epoch of comet and giant planet formation

P. Hily-Blant<sup>1,2</sup>, V. Magalhaes de Souza<sup>3</sup>, J. Kastner<sup>4</sup>, and T. Forveille<sup>2</sup>

<sup>1</sup> Institut Universitaire de France e-mail: pierre.hily-blant@univ-grenoble-alpes.fr

<sup>2</sup> Univ. Grenoble Alpes, CNRS, IPAG, 38000 Grenoble, France

<sup>3</sup> IRAM, 300 rue de la Piscine, Grenoble, France

<sup>4</sup> Chester F. Carlson Center for Imaging Science, School of Physics & Astronomy, and Laboratory for Multiwavelength Astrophysics, Rochester Institute of Technology, 54 Lomb Memorial Drive, Rochester NY 14623 USA

## ABSTRACT

The isotopic ratio of nitrogen measured in primitive solar system bodies shows a large extent of values, the origin of which remain unknown. One key question is whether the isotopic reservoirs of nitrogen found in cosmomaterials are already present at, or posterior to, the comet formation stage. Another central question is to elucidate the processes capable of producing the observed variations of the  $^{14}\text{N}/^{15}\text{N}$  isotopic ratio. Disks orbiting pre-main-sequence (TTauri) stars provide unique opportunities to observe the chemical content of analogs of the protosolar nebula and therefore to build a comprehensive scenario explaining the origin of nitrogen in the solar system and in planet-forming disks. With ALMA, it has become possible to measure isotopic ratios of nitrogen-bearing species in such environments. We present spectrally and spatially resolved observations of the hyperfine structure of the 4-3 rotational transition of HCN and its main isotopologues  $\text{H}^{13}\text{CN}$ , and  $\text{HC}^{15}\text{N}$ , in the disk orbiting the 8 Myr-old TTauri star TW Hya. The sensitivity allows the  $\text{HCN}/\text{H}^{13}\text{CN}$  and  $\text{HCN}/\text{HC}^{15}\text{N}$  abundance ratios to be measured directly, under minimal assumptions. The spatially averaged ratios are  $86\pm 4$  and  $223\pm 21$  respectively. The latter result, when compared with the directly measured  $\text{CN}/\text{C}^{15}\text{N}$  ratio of  $323\pm 30$  in this disk, provides clear-cut evidence that two isotopic reservoirs of nitrogen are present in this disk at the stage of giant-planet and comet formation. Furthermore, we find that the  $\text{HCN}/\text{HC}^{15}\text{N}$  ratio increases from  $121\pm 11$  to  $339\pm 28$  as the radius increases from 20 to 45 au. This finding lends support to selective photo-dissociation of  $\text{N}_2$  being the dominant fractionation process.

**Key words.** Astrochemistry; ISM: abundances; Individual objects: TW Hya

## 1. Introduction

Isotopic ratios of nitrogen in various bodies of the solar system (meteorites, comets, planets, etc) show the largest variations among the most abundant constituents (carbon, oxygen), with  $^{14}\text{N}/^{15}\text{N}$  ratios ranging from  $\sim 50$  in sub- $\mu\text{m}$  grains immersed in chondrites matrix (so-called hotspots) to 441 in the Sun and Jupiter (Bonal et al. 2010; Marty et al. 2011; Fouchet et al. 2000; Hily-Blant et al. 2013). When, where, and how, these isotopic reservoirs of nitrogen formed during the evolution from a molecular cloud to planetary systems remains to be determined. Comets provide a special case among primitive cosmomaterials: regardless of the cometary type (short or long period) or of the carrier of nitrogen observed in their coma (CN, HCN,  $\text{NH}_2$ ,  $\text{NH}_3$ ,  $\text{N}_2$ , NO), the isotopic ratio is consistently found to be  $\approx 140$  (Wampfler et al. 2018; Hily-Blant et al. 2017, hereafter HB17, and references therein), a factor three lower than the elemental ratio—that is, the ratio of the bulk Sun—of 441. There is still no explanation for this well established observational fact.

Evolved protoplanetary disks at the stage of giant planet and comet formation provide unique opportunities to investigate the origin of this  $^{15}\text{N}$ -rich reservoir of nitrogen. The nitrogen isotopic ratio was measured via rare isotopologues<sup>1</sup> of  $\text{H}^{12}\text{C}^{14}\text{N}$ —specifically,  $\text{H}^{13}\text{CN}$  and  $\text{HC}^{15}\text{N}$ —for a small sample of disks with the ALMA interferometer (Guzmán et al. 2017), yielding

$\text{HCN}/\text{HC}^{15}\text{N}$  ratios between  $83\pm 32$  and  $156\pm 71$  (Guzmán et al. 2017), and a mean value of  $111\pm 19$ . This constituted the first hint of a  $^{15}\text{N}$ -enriched reservoir of nitrogen in analogs of the protosolar nebula (PSN). However, a direct  $\text{HCN}/\text{HC}^{15}\text{N}$  was needed to confirm this result. A direct measurement of the  $\text{CN}/\text{C}^{15}\text{N}$  ratio,  $323\pm 30$ , was indeed performed in the TW Hya system (HB17). This value was proposed to indicate the present-day ratio in the bulk solar neighborhood, significantly lower than the elemental ratio in the PSN, but in excellent agreement with Galactic Chemical Evolution (GCE) model predictions (Romano et al. 2017). Moreover, the different HCN and CN ratios provided the first indication of two isotopic reservoirs of nitrogen existing at the time of comet formation. However,  $\text{HCN}/\text{HC}^{15}\text{N}$  was not measured in TW Hya such that a clear-cut evidence of two distinct reservoirs was lacking.

To elucidate the origin of nitrogen in the solar system requires the processes leading to the  $^{14}\text{N}/^{15}\text{N}$  isotopic ratio variations to be identified (Hily-Blant et al. 2013, 2017; Füre & Marty 2015). The efficiency of chemical mass fractionation, the only process expected in cold and shielded gas (Terzieva & Herbst 2000), has recently been called into question both theoretically (Roueff et al. 2015; Wirstrom & Charnley 2018) and observationally by measuring the  $\text{HCN}/\text{HC}^{15}\text{N}$  ratio in the L1498 pre-stellar core (Magalhães et al. 2018). The obtained value,  $338\pm 28$ , is in excellent agreement with the present-day elemental ratio of  $\sim 330$  proposed by HB17, thus supporting the prediction that chemical fractionation is not an efficient process even in

<sup>1</sup> Hereafter, the three isotopologues  $\text{H}^{12}\text{C}^{14}\text{N}$ ,  $\text{H}^{13}\text{C}^{14}\text{N}$ , and  $\text{H}^{12}\text{C}^{15}\text{N}$ , are denoted HCN,  $\text{H}^{13}\text{CN}$ , and  $\text{HC}^{15}\text{N}$ , respectively.

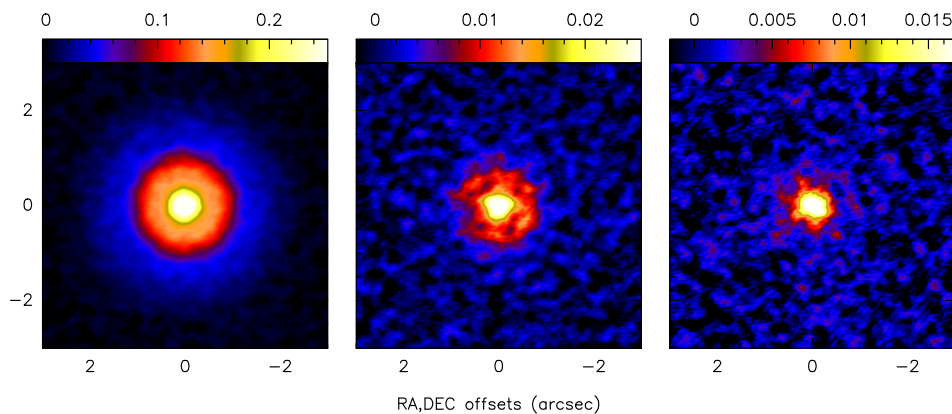


**Fig. 1.** Integrated intensity maps ( $\text{Jy/beam km s}^{-1}$ ) of HCN,  $\text{H}^{13}\text{CN}$ , and  $\text{HC}^{15}\text{N}$  (from left to right). The emission was integrated over  $5 \text{ km s}^{-1}$  for HCN and  $2 \text{ km s}^{-1}$  for the less abundant isotopologues, centered at on the systemic velocity of  $2.83 \text{ km s}^{-1}$ . The maps are centered at  $\alpha = 11:01:51.81150$ ,  $\delta = -34:42:17.2636$  (J2000.0). The visibilities were projected on the same spatial grid and convolved to a synthesized beam of HPBW  $0.26'' \times 0.21''$ . The distance to TW Hya is  $59.5 \pm 0.9 \text{ pc}$  (GAIA DR2).

cold pre-stellar cores. Further credence was provided by subsequent direct measurements in  $\text{HC}_3\text{N}$  and  $\text{HC}_5\text{N}$  towards similar sources (Hily-Blant et al. 2018; Taniguchi & Saito 2017). Yet, the concordance between observations and models may be only an apparent one, because sharp deviations are recurrently obtained for  $\text{N}_2\text{H}^+$  (Bizzocchi et al. 2013; Redaelli et al. 2018).

The other fractionation process, selective photo-dissociation of  $\text{N}_2$ , expected in unshielded gas, has been investigated in the context of protoplanetary disks and molecular clouds (Heays et al. 2014; Visser et al. 2018; Furuya & Aikawa 2018). The opacity of  $\text{N}^{15}\text{N}$  being much smaller than that of  $\text{N}_2$ , more  $^{15}\text{N}$  atoms are released upon dissociation than  $^{14}\text{N}$ , leading to an atomic isotopic ratio lower than the bulk. Gas-phase and/or surface chemistry then propagates this deviation into other species. One thus expects a correlation (positive or negative) between the UV flux and the  $^{14}\text{N}/^{15}\text{N}$  ratio in some species. For HCN in disks, the HCN/ $\text{HC}^{15}\text{N}$  ratio is predicted to increase with decreasing UV flux.

In this Letter, we aim at providing the requisite evidence for two distinct N reservoirs within the disk orbiting the nearby T Tauri star TW Hya, via analysis of the emission of HCN and isotopologues, based on archival ALMA data (2016.1.00629.S, Cleeves et al). We also explore the possibility of a radial gradient in the HCN/ $\text{HC}^{15}\text{N}$  ratio, so as to test whether selective photo-dissociation is the driving fractionation process in PSN analogs.

## 2. Observations and data reduction

The (4-3) rotational transitions of HCN,  $\text{H}^{13}\text{CN}$ , and  $\text{HC}^{15}\text{N}$  at 354.5, 345.4, and 344.2 GHz respectively, have been mapped with the ALMA interferometer with a spectral resolution of 61 KHz or  $0.053 \text{ km s}^{-1}$  (see App. A). All the lines were observed simultaneously, thus mitigating cross-calibration biases. The standard pipeline of CASA 5.4.0 was used to generate the complex visibilities which were then self-calibrated in Gildas<sup>2</sup>. The final sensitivities are 2.3, 1.9, and  $2.0 \text{ mJy/beam per } 0.053 \text{ km s}^{-1}$  spectral channel, for HCN,  $\text{H}^{13}\text{CN}$ , and  $\text{HC}^{15}\text{N}$  respectively. The resulting integrated intensity maps are shown in Fig. 1.

The HCN(4-3) spectra (see Fig. 2) consist in two weak hyperfine (hf) transitions of equal intensity, each carrying 2.1% of the total intensity, and shifted by  $-1.672$  and  $+1.360 \text{ km s}^{-1}$  with respect to our reference frequency  $354505.477 \text{ MHz}$ . They surround a strong, non-Gaussian, central feature made of three overlapping hf transitions representing 95.8% of the flux. Regarding  $\text{H}^{13}\text{CN}$  and  $\text{HC}^{15}\text{N}$ , their intrinsically weaker intensity

<sup>2</sup> IRAM memo available at <http://www.iram.fr/IRAMFR/ARC/documents/filler/casa-gildas.pdf>.

compared to HCN leads to one single feature only which, in the case of  $\text{H}^{13}\text{CN}$ , carries 95.8% of the total flux. For  $\text{HC}^{15}\text{N}$ , the splitting is entirely not resolved and the single feature carries 100% of the power of the rotational transition (see Table A.1).

## 3. Results

The conversion of line flux into abundance ratios is a simple procedure provided the lines are optically thin and the excitation temperatures are known. Yet, even for optically thin transitions, the overlap, in velocity space, of lines emitted at different locations in the disk—a result of the Keplerian rotation of the disk—complicates the conversion from flux to abundance ratios because this mixes different regions of the disk, broadens the lines, and may also weaken the assumption that the emitting species are co-spatial. The latter is especially true in the case of species with very different abundances, such as nitrogen isotopologues. Mitigating both the optical depth and Keplerian blurring effects thus offers serious advantages.

The nearly face-on configuration of the TW Hya disk naturally reduces the Keplerian blurring. Although emerging lines carry the contribution from different locations along the line of sight, the spatial mixing is limited to the vertical direction. Moreover, the spectrally resolved hyperfine multiplet of HCN provides two weak lines that are most likely optically thin. Their flux is thus directly proportional to their column density.

Because the emission of all three isotopologues is well detected and spatially resolved, one goal could be to measure the HCN isotopic ratios as a function of radius, provided that line broadening can be minimized. This implies limiting the spatial area over which spectra are averaged. Another, complementary, approach consists in deriving a spatially averaged isotopic ratio by measuring line flux ratios over the whole disk. This method provides higher sensitivity, but Keplerian line broadening must still be controlled. Both approaches have been applied and are detailed in the following.

### 3.1. Spatially averaged line fluxes

In order to limit the Keplerian line broadening, the spectra are averaged over several groups of pixels selected for their closely similar projected Keplerian velocity. In practice, a 2D mask is thus determined by selecting, in each velocity channel, the disk area where the  $354507.455 \text{ MHz}$  hf emission of HCN is above  $40 \text{ mJy/beam}$ . Although the overlap of different Keplerian velocities is well controlled, it is still important close to the disk center, and we further masked out the spectra located at radii smaller than  $0.3''$ . The resulting mask recovers the usual dipole-

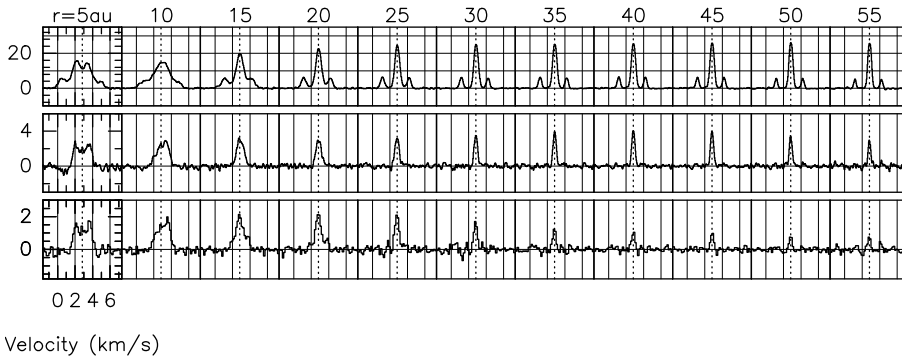


**Fig. 2.** Spectra of HCN, H<sup>13</sup>CN, and HC<sup>15</sup>N (from top to bottom) from the Keplerian mask at 2.83 km s<sup>-1</sup> (systemic velocity) and averaged within annuli centered at radii  $r = 5$  to 55 au. The specific intensity scale is K using K/(Jy/beam) conversion factors of 178.7, 188.1, and 189.0 for HCN, H<sup>13</sup>CN, and HC<sup>15</sup>N, respectively.

like pattern, but with a central hole due to the radial filter (see Fig. B.1). As a result, the spectra averaged within each Keplerian velocity mask have a high signal-to-noise ratio (see Fig. B.2), allowing the two weak hf transitions of HCN to be properly fitted. The line fluxes of the two weak hf lines at 354503.869 and 354507.455 MHz have been measured through Gaussian fitting and their averaged value, corrected by their summed relative intensity (4.2%), is then used as an estimator of the HCN flux (see Table B.1).

### 3.2. Radially dependent fluxes

In order to measure the flux ratios as a function of distance from the central T Tauri star, and still avoid Keplerian line-broadening, a radial mask was superimposed on the previously described Keplerian masks. Spectra contained within concentric annuli, centered at radii  $r = 5$  to 55 au by step of 5 au (1/3rd of the HPBW), and of constant thickness  $\delta r = 5$  au, were averaged. The outer radius is imposed by the HC<sup>15</sup>N detection limit (see Fig. 1). The number of spectra in each annulus increases with  $r$ , which compensates for the natural decrease of the signal-to-noise with radius. In the process, spectra were weighted according to their flux rms. As in the spatially averaged approach, the line flux of HCN, H<sup>13</sup>CN, and HC<sup>15</sup>N, were measured through Gaussian fitting.

Radially averaged spectra corresponding to the Keplerian mask at 2.83 km s<sup>-1</sup> are shown in Fig. 2, where the velocity confusion at small radii is evident, while at radii above 20 au, it is efficiently removed by our masking procedure. Average spectra in all Keplerian channels are visible in Fig. B.3. While the peak intensity of HCN hardly changes beyond 20 au, this of H<sup>13</sup>CN and HC<sup>15</sup>N decrease when moving outwards. Also, all lines become narrower as the radius increases (see Table B.3). For HCN, the FWHM is  $1.5 \pm 0.7$  km s<sup>-1</sup> at  $r \leq 0.2''$ , decreasing to  $0.34 \pm 0.02$  km s<sup>-1</sup> at  $0.9''$ .

## 4. Isotopic ratios

Because the three molecules have very similar spectroscopic constants, their rotational flux ratios are equal to their column density ratios to within 1%, provided the lines are optically thin and have the same excitation temperature. Under such assumptions, that we shall verify later, we obtain the isotopic ratios directly from the fluxes. The results are shown in Fig. 3.

For HCN/HC<sup>15</sup>N, we find ratios between 185 to 252 across the Keplerian channels (typical uncertainty of 5-10%) with an average isotopic ratio  $R_2 = 223 \pm 21$ . Here and elsewhere, uncertainties on the absolute flux include a conservative 10% (statistical) from amplitude calibration. The quoted uncertainty on average values is the largest of the weighted uncertainties and

**Table 1.** Isotopic ratios derived from our two approaches the spatially averaged and radially dependent methods (see also Fig. 3).

	HCN/HC <sup>15</sup> N	HCN/H <sup>13</sup> CN	H <sup>13</sup> CN/HC <sup>15</sup> N
Average	223±21	86±4	2.6±0.2
$r$ (au)=20	121.4±10.6	85.6± 5.2	1.4±0.1
25	140.4±14.6	84.2± 5.7	1.7±0.1
30	176.4±24.1	75.9± 7.0	2.4±0.3
35	248.7±24.6	77.9± 5.5	3.2±0.4
40	307.8±14.2	81.2± 4.8	3.7±0.3
45	338.7±28.2	82.5± 4.2	4.2±0.4
50	334.9±55.0	85.9± 5.9	3.9±0.7
55	256.4±91.2	88.7±11.1	2.9±1.1

the dispersion of the averaged values. The lowest values (185, 186, 198) are obtained in the three central Keplerian channels, and the average ratio in the 8 remaining channels is  $233 \pm 12$ . The HCN/H<sup>13</sup>CN isotopic ratio is more uniform, with values ranging from 82 to 92, averaging to  $86 \pm 4$ . The corresponding H<sup>13</sup>CN/HC<sup>15</sup>N average ratio is  $2.6 \pm 0.2$ , with values ranging from 2.22 to 2.75. The low values of the HCN/HC<sup>15</sup>N ratio could be due to the opacity of HCN being substantial even in its weak hf lines: indeed, the HC<sup>15</sup>N flux in these channels increases while that of HCN remains uniform. Assuming a constant isotopic ratio of 233, and adopting, for the opacity correction to the integrated intensity, the usual expression  $\tau/(1 - \exp(-\tau))$  with  $\tau$  the opacity (Goldsmith & Langer 1999), an opacity of 0.38 for the weakest hf lines—corresponding to a rotational opacity  $\tau_{12} \approx 20$ —would be needed to explain the flux ratios in these three channels. Alternatively, assuming a constant H<sup>13</sup>CN/HC<sup>15</sup>N ratio of 2.66 based on the outer channels, the total H<sup>13</sup>CN opacity would be  $\tau_{13} = 0.3$  in the three middle channels, corresponding to  $\tau_{12} = 86 \times 0.3 = 26$ . It is thus likely that the opacity of the weakest hf line of HCN(4-3) and of H<sup>13</sup>CN(4-3) is  $\approx 0.3$ , i.e. not totally negligible, but still fulfilling our optically thin assumption. We note that in those three channels, the HCN/H<sup>13</sup>CN ratio would change by less than 4% if applying these corrections.

The radially dependent approach shows that the HCN/HC<sup>15</sup>N isotopic ratio varies with radius while the HCN/HC<sup>13</sup>CN remains constant within  $1\sigma$ . More specifically, the former ratio increases from 121 at 20 au to 338 at 45 au, and then decreases at larger distances. The nitrogen isotopic ratio in HCN close to the star is thus a factor 2.7 lower than the spatially averaged CN/C<sup>15</sup>N ratio,  $323 \pm 30$ , whereas from 45 to 50 au, the two ratios become consistent within  $1\sigma$ . The increase of HCN/HC<sup>15</sup>N is consistent with a power-law steeper

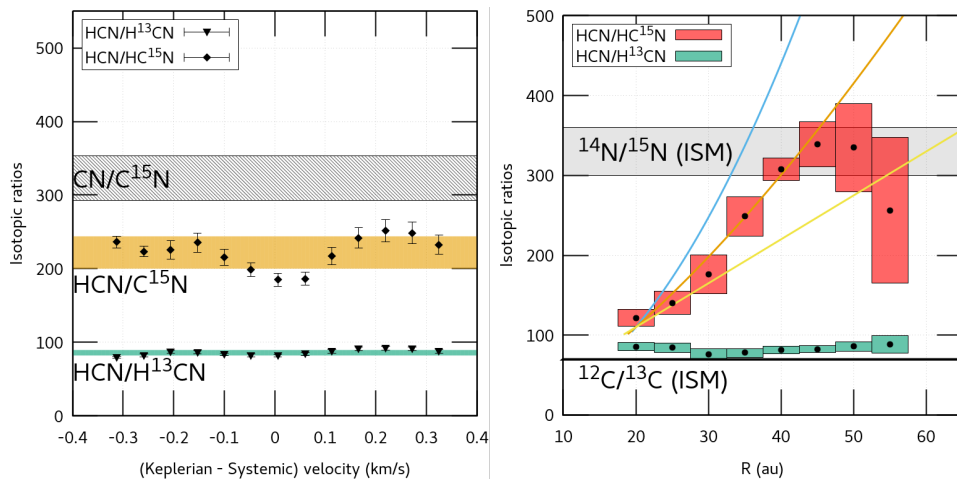


**Fig. 3.** **Left:** HCN/HC<sup>15</sup>N and HCN/H<sup>13</sup>CN isotopic ratios in each Keplerian channel derived from the spatially averaged procedure (see Sect. 3.1). The colored bands indicate the average value  $\pm 1\sigma$ . The spatially averaged CN/C<sup>15</sup>N ratio from HB17 is shown as a hatched rectangle. **Right:** radial dependence (see Sect. 3.2) of the HCN/H<sup>13</sup>CN and HCN/HC<sup>15</sup>N ratios. The width of each box is 5 au (1/3rd of the HPBW) and the height indicates the  $\pm 1\sigma$  uncertainties. The full lines show power-laws of exponents 1, 1.45, and 2. The shaded area and the horizontal lines are the present-day <sup>14</sup>N/<sup>15</sup>N and <sup>12</sup>C/<sup>13</sup>C elemental ratios ( $330 \pm 30$  and 70, respectively).

than a linear growth, with a best-fit exponent of 1.45, although a sharper dependence can not be ruled out.

A key assumption in our analysis is that of a single excitation temperature characterizing the weak hf lines of HCN and the overlapping hf lines of H<sup>13</sup>CN and of HC<sup>15</sup>N. Yet, the overlapping hf lines of HCN may lead to unequal excitation temperatures Magalhães et al. (2018). We have tested our assumption (see App. C) by computing the excitation temperatures of HCN, H<sup>13</sup>CN, and HC<sup>15</sup>N lines while taking into account line overlap in the excitation. We assumed uniform physical conditions covering density and gas temperature regimes from  $10^6$  to  $10^{11}$  cm<sup>-3</sup> and 5 to 30 K, respectively. We found that deviations from a single excitation temperature are only obtained at densities below  $3 \cdot 10^7$  cm<sup>-3</sup> (see Fig. C.1). On the other hand, the FWHM of the HCN, H<sup>13</sup>CN, and HC<sup>15</sup>N lines, at a radius of  $0.6''$  ( $\approx 35$  au) and beyond, is  $\approx 0.35$  km s<sup>-1</sup>, which places an upper limit on the kinetic temperature of  $(FWHM/2.35)^2 \times \mu m_H / (2k_B) \approx 35$  K (Teague et al. 2016). Referring to the TW Hya model of van't Hoff et al. (2017), this upper limit indicates that the density is, at such radii, larger than  $10^9$  cm<sup>-3</sup>, i.e. in a regime where lines should be thermalized, thus validating our basic assumption. Our upper limit on the kinetic temperature is also well below the gas temperature of  $\sim 200$  K where the HCN abundance is the highest in the generic models of Visser et al. (2018).

## 5. Discussion

The spatially averaged, directly measured CN/C<sup>15</sup>N and HCN/HC<sup>15</sup>N ratios in the TW Hya circumstellar disk provide clear-cut confirmation of at least two isotopic reservoirs of nitrogen, as anticipated by HB17. In CN, the ratio is  $1.4 \pm 0.2$  times larger than in HCN, and their difference is  $90 \pm 36$ . Given the  $\sim 8$  Myr age of TW Hya, these results indicate that multiple isotopic reservoirs are present at the key protoplanetary disk evolutionary stages when comets and giant planets are likely forming.

In the comet formation zone between 20 and 30 au, we find HCN gas that is enriched in <sup>15</sup>N by a factor of 2.8 compared to the bulk ISM, reminiscent of the threefold <sup>15</sup>N-enrichment of comets compared to the bulk Sun. This provides strong indication that HCN traces the fractionated reservoir recorded by comets. We also note the value of  $121 \pm 11$  confirms the mean HCN/HC<sup>15</sup>N ratio of  $111 \pm 19$  (HB17) obtained indirectly by Guzmán et al. (2017) assuming HCN/H<sup>13</sup>CN =  $70 \pm 20$ . Adopting our measured averaged of 86 for the latter would bring the former ratio to  $136 \pm 23$ . Furthermore, at larger radii, the nitrogen

reservoir traced by HCN is no longer fractionated, with an isotopic ratio consistent with both that of CN and with the revised elemental ratio of 330. The latter value is based on direct measurements from nearby low-mass star forming regions and the agreement with the HCN gas at 55 au confirms the idea of an interstellar, not fractionated, nitrogen gas at large radii in PNS analogs. Yet, a final decrease of the ratio beyond 55 au is noticeable although not statistically significant, which could indicate chemical processes in a UV-shielded gas where depletion is limited. Direct, high signal-to-noise ratio measurements beyond 60 au are needed to build a clear picture.

The average HCN/H<sup>13</sup>CN ratio,  $86 \pm 4$ , is significantly larger than the <sup>12</sup>C/<sup>13</sup>C ratio of  $\approx 65$  in the local ISM (Halfen et al. 2017), but is in surprisingly good agreement with the value of 90 in the protosolar nebula. The high ratio found in TW Hya indicates that HCN is depleted in <sup>13</sup>C, while it was found to be enriched in the L1498 pre-stellar core (Magalhães et al. 2018), suggesting that the underlying process may not be the same in these two environments. Optically thick H<sup>13</sup>CN emission could artificially increase the HCN/H<sup>13</sup>CN ratio provided that the weak HCN hf transition remains thin. However, the H<sup>13</sup>CN opacity needed to bring down the ratio to the elemental value is 0.55, which is larger than the value of 0.3 derived previously for the central Keplerian channels. Also, this would imply that the total opacity of HCN would be 35, and that of the weakest HCN hf line would be 0.75, twice larger than the value of 0.38 needed to bring the spatially averaged HCN/HC<sup>15</sup>N ratio to a constant value (see Sec. 4). We note that high <sup>12</sup>C/<sup>13</sup>C ratios have already been measured in carbon monoxide from ices towards YSOs (Smith et al. 2015). The depletion of HCN in <sup>13</sup>C is however at variance with the models of Visser et al. (2018) which predict instead that HCN is enriched in <sup>13</sup>C at radii below  $\sim 100$  au.

Nevertheless, the increasing HCN/HC<sup>15</sup>N ratio with radius may indicate that selective photo-dissociation represents the dominant fractionation process in disks (Visser et al. 2018). In these models, the HCN/HC<sup>15</sup>N column density ratio first decreases with radius before increasing back to the elemental ratio as a consequence of UV flux attenuation due to a combination of geometrical dilution and dust extinction. We note that the minimum ratio in the grid of models of Visser et al. (2018) is  $\approx 240$ – $280$  for disks around TTauri stars, which would translate down to  $180$ – $210$  if one assumes 330 (rather than 441) for the elemental ratio, hence still larger than the lowest ratio reported here. This could indicate that the UV flux is underestimated in these models. However, dedicated models of TW Hya should be performed as the precise radial dependence of the isotopic ratio

strongly depends on the physical parameters of the model (disk mass, grain size and dust:gas mass ratio).

*Acknowledgements.* PHB thanks D. Petry for his help in processing the ALMA data, and A. Faure for useful comments and discussions. We also thank the referee and the editor for valuable comments that greatly clarified the paper. This study makes use of the ADS/JAO.ALMA#2016.1.00629.S data. ALMA is a partnership of ESO (representing its member states), NSF (USA) and NINS (Japan), together with NRC (Canada), MOST and ASIAA (Taiwan), and KASI (Republic of Korea), in cooperation with the Republic of Chile. The Joint ALMA Observatory is operated by ESO, AUI/NRAO and NAOJ. This work has been supported by a grant from Labex OSUG@2020. JHK's research on protoplanetary disks orbiting young stars near Earth is supported by NASA Exoplanets Research Program grants NNX16AB43G and 80NSSC19K0292 to RIT. This study made use of the CDMS database (Müller et al. 2005).

## References

- Beckwith, S. V. W. & Sargent, A. I. 1993, *ApJ*, 402, 280  
Bizzocchi, L., Caselli, P., Leonardo, E., & Dore, L. 2013, *A&A*, 555, A109  
Bonal, L., Huss, G. R., Krot, A. N., et al. 2010, *GCA*, 74, 6590  
Daniel, F. & Cernicharo, J. 2008, *A&A*, 488, 1237  
Fouchet, T., Lellouch, E., Bézard, B., et al. 2000, *Icarus*, 143, 223  
Füri, E. & Marty, B. 2015, *Nature Geosci.*, 8, 515  
Furuya, K. & Aikawa, Y. 2018, *ApJ*, 857, 105  
Goldsmith, P. F. & Langer, W. D. 1999, *ApJ*, 517, 209  
Guzmán, V. V., Öberg, K. I., Huang, J., Loomis, R., & Qi, C. 2017, *ApJ*, 836, 30  
Halfen, D. T., Woolf, N. J., & Ziurys, L. M. 2017, *ApJ*, 845, 158  
Heays, A. N., Visser, R., Gredel, R., et al. 2014, *A&A*, 562, A61  
Hily-Blant, P., Bonal, L., Faure, A., & Quirico, E. 2013, *Icarus*, 223, 582  
Hily-Blant, P., Faure, A., Vastel, C., et al. 2018, *MNRAS*, 480, 1174  
Hily-Blant, P., Magalhaes, V., Kastner, J., et al. 2017, *A&A*, 603, L6  
Magalhães, V. S., Hily-Blant, P., Faure, A., Hernandez-Vera, M., & Lique, F. 2018, *A&A*, 615, A52  
Marty, B., Chaussidon, M., Wiens, R. C., Jurewicz, A. J. G., & Burnett, D. S. 2011, *Science*, 332, 1533  
Müller, H. S. P., Schlöder, F., Stutzki, J., & Winnewisser, G. 2005, *Journal of Molecular Structure*, 742, 215  
Redaelli, E., Bizzocchi, L., Caselli, P., et al. 2018, *ArXiv e-prints* [[arXiv:1806.01088](https://arxiv.org/abs/1806.01088)]  
Romano, D., Matteucci, F., Zhang, Z.-Y., Papadopoulos, P. P., & Ivison, R. J. 2017, *MNRAS*, 470, 401  
Roueff, E., Loison, J. C., & Hickson, K. M. 2015, *A&A*, 576, A99  
Smith, R. L., Pontoppidan, K. M., Young, E. D., & Morris, M. R. 2015, *The Astrophysical Journal*, 813, 120  
Taniguchi, K. & Saito, M. 2017, *PASJ*, 69, L7  
Teague, R., Guilloteau, S., Semenov, D., et al. 2016, *A&A*, 592, A49  
Terzieva, R. & Herbst, E. 2000, *MNRAS*, 317, 563  
van't Hoff, M. L. R., Walsh, C., Kama, M., Facchini, S., & van Dishoeck, E. F. 2017, *A&A*, 599, A101  
Visser, R., Bruderer, S., Cazzoletti, P., et al. 2018, *A&A*, 615, A75  
Wampfler, S., Rubin, M., Altwegg, K., et al. 2018, in *COSPAR Meeting*, Vol. 42, 42nd COSPAR Scientific Assembly, B1.3–21–18  
Wirström, E. S. & Charnley, S. B. 2018, *MNRAS*, 474, 3720



## Appendix A: Observations

The observations were performed with the ALMA interferometer (2016.1.00629.S, PI: I. Cleeves) and spread over 6 epochs (30/12/2016, 05/07/2017, 10/07/2017, 15/07/2017, 21/07/2017, 22/07/2017). J1037-2934 was used as a bandpass, flux, and phase calibrator. The phase was also calibrated with J1103-3251, while J1058+0133 was also used for bandpass calibration.

$\text{H}^{13}\text{CN}$  and  $\text{HC}^{15}\text{N}$  were tuned in the lower side band and HCN in the upper side band, allowing simultaneous observations for the three species. We used the standard pipeline of CASA 5.4.0 to generate the first sets of complex visibilities which were then exported into the Gildas format using the Gildas-Casa filer of Guilloteau, Chapillon et al (see the IRAM memo available at <http://www.iram.fr/IRAMFR/ARC/documents/filler/casa-gildas.pdf>). Self-calibration was then applied to generate the final set of visibilities.

As can be seen from Table A.1, three hyperfine (hf) transitions of HCN(4-3) are separated by less than  $0.13 \text{ km s}^{-1}$  and are not resolved. Their total relative intensity is 95.8%. The hf transition at 354505.846 MHz is not detected given its 0.03% relative strength. The properties of the hf lines of HCN and  $\text{H}^{13}\text{CN}$  are summarized in Table A.1, while for  $\text{HC}^{15}\text{N}$ , the unresolved hyperfine splitting is not given. We also show in Fig. B.1 channel maps of HCN strong central feature,  $\text{H}^{13}\text{CN}$ , and  $\text{HC}^{15}\text{N}$ . The velocity range covers the main, and overlapping, hf lines, of HCN.

**Table A.1.** Spectroscopic information on the observed transitions.

Rest Freq. <sup>a</sup> MHz	$\delta v^b$ $\text{km s}^{-1}$	$A_{ul}^c$ $\text{s}^{-1}$	$g_u^d$	R. I. <sup>e</sup>
<b>HCN</b>				
354503.869	1.360	1.284 (-4)	9	2.083 (-2)
354505.367	0.094	1.886 (-3)	7	2.381 (-1)
354505.477	0.000	1.925 (-3)	9	3.125 (-1)
354505.523	-0.039	2.054 (-3)	11	4.075 (-1)
354505.846	-0.312	2.620 (-6)	7	3.307 (-4)
354507.455	-1.672	1.650 (-4)	7	2.083 (-2)
<b><math>\text{H}^{13}\text{CN}</math></b>				
345338.160	-1.398	1.190 (-4)	9	2.089 (-2)
345339.660	-0.095	1.740 (-3)	7	2.376 (-1)
345339.770	0.000	1.780 (-3)	9	3.125 (-1)
345339.810	0.035	1.900 (-3)	11	4.077 (-1)
345340.140	0.321	2.420 (-6)	7	3.305 (-4)
345341.750	1.719	1.530 (-4)	7	2.089 (-2)
<b><math>\text{HC}^{15}\text{N}</math></b>				
344200.109	0.000	1.8793 (-3)	9	1

NOTE.—Numbers are written in the form  $a(b) = a \times 10^b$ .

<sup>a</sup> Rest frequency. <sup>b</sup>  $\delta v$  is the velocity shift of each hf transition within a given multiplet.

<sup>c</sup> Coefficient for spontaneous decay.

<sup>d</sup> Upper level total degeneracy.

<sup>e</sup> The relative intensity of each hf line, normalized to a sum of 1.

## Appendix B: Keplerian masks

### Appendix B.1: Results from the spatially averaged procedure

In Fig. B.1 (top row), we show the Keplerian mask defined as explained in the main text. Each mask is overlaid in the channel maps of the three isotopologues, showing the usual dipole-like pattern (Beckwith & Sargent 1993). Comparing the rows showing the main feature and the weak hf line of HCN, we note that the extended HCN emission is filtered out in the present study, as is the case of  $\text{H}^{13}\text{CN}$ , although to a lesser extent. The spectra averaged within each mask, shown in Fig. B.2, have been fitted with Gaussian profiles, the results of which are summarized in Table B.1. The obtained fluxes are then used to derive the *spatially averaged* isotopic ratios listed in Table B.2.

### Appendix B.2: Radial dependence procedure

By combining two masks, one in velocity space (Keplerian mask) and one in the radial direction, we are able to study the radial dependence of the  $^{14}\text{N}/^{15}\text{N}$  isotopic ratio in HCN towards the TW Hya system. In Fig. 2, we show the spectra averaged within each annulus, while limiting ourselves to the central Keplerian channel at  $2.83 \text{ km s}^{-1}$  (systemic velocity). Figure B.3 is complementary in that it shows the spectra averaged at three radii, but within all Keplerian masks.

As in the radially averaged approach, the spectral line intensity and shape at any radius does not change appreciably among the various Keplerian velocity channels. In contrast, there is a significant dependence with radius, especially for  $\text{H}^{13}\text{CN}$  and most importantly for  $\text{HC}^{15}\text{N}$ . As can be seen in Table B.3, and as mentioned in the main text, all lines become narrower as the radius increases (see Table B.3).

### Appendix B.3: Radially dependent line width

Gaussian fits to Keplerian-filtered spectra averaged within concentric annuli of thickness  $0.1''$  have been performed in order to measure the dependence of the FWHM of the HCN,  $\text{H}^{13}\text{CN}$ , and  $\text{HC}^{15}\text{N}$  lines. The results are summarized in Table B.3. They are used to infer an upper limit on the kinetic temperature following HB17 and Teague et al. (2016).

## Appendix C: Single excitation temperature assumption

The main assumption in our analysis is that of a single excitation temperature characterizing the weak hf lines of HCN and the overlapping hf lines of  $\text{H}^{13}\text{CN}$  and of  $\text{HC}^{15}\text{N}$ . A thorough investigation of this assumption can only be done with two-dimensional radiative transfer taking into account the overlap of hf transitions in the level population evaluation, which in turn requires a complete physical and kinematic structure of the disk. This type of analysis has been done in the context of pre-stellar, starless, cores by Magalhães et al. (2018), in a spherical geometry, with the 1D ALICO model (Daniel & Cernicharo 2008).

In the present context, such detailed calculations could not be performed. Instead, we used our 1D ALICO code to investigate the density and kinetic gas temperature at which departures from the single excitation temperature assumption may be obtained. To do so, the level populations were computed while treating the effect of hf line overlap in the excitation of HCN,  $\text{H}^{13}\text{CN}$ , and  $\text{HC}^{15}\text{N}$ . Our grid of models encompasses a range

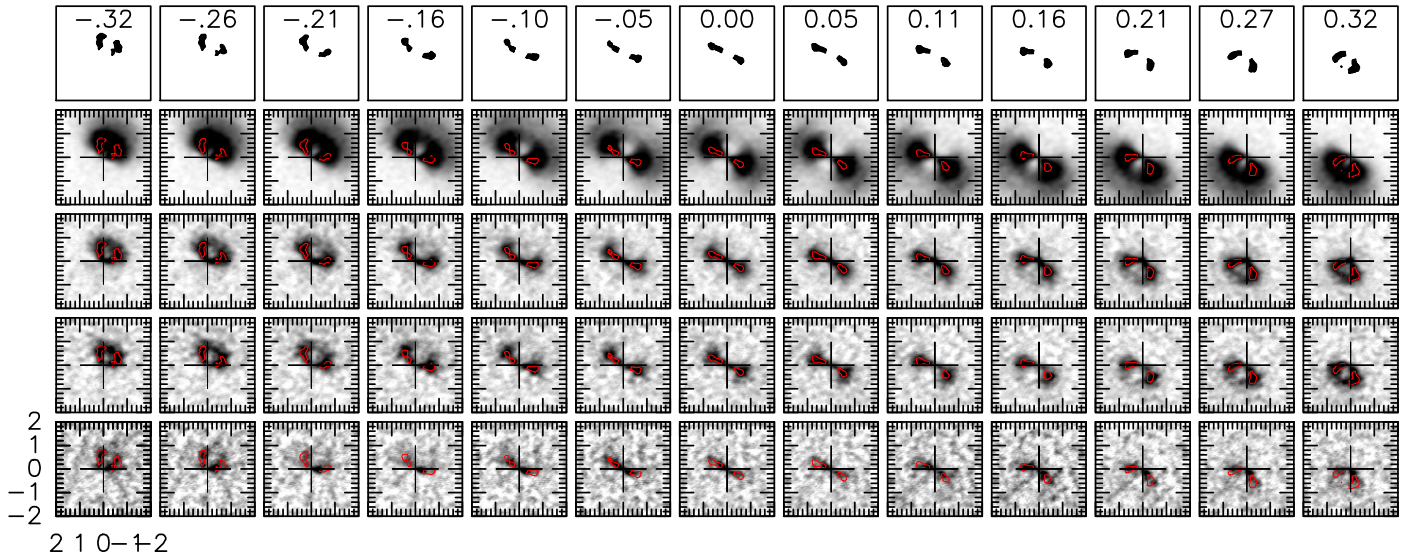


**Fig. B.1.** Keplerian masks (top row) overlaid on (from top to bottom) the HCN (main feature and weak hf line at 345507.455 MHz),  $\text{H}^{13}\text{CN}$ , and  $\text{HC}^{15}\text{N}$ , channel maps. The masks (top row) were obtained for a threshold of 40 mJy/beam applied to the weak hf transition at 345507.455 MHz.

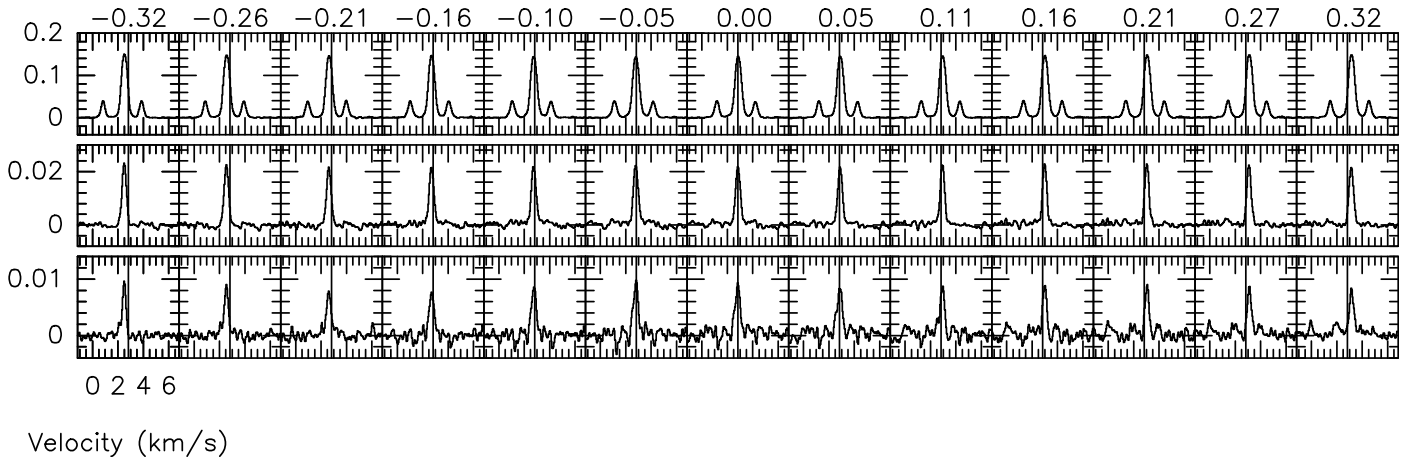


**Fig. B.2.** Spatially averaged spectra (Jy/beam) within each Keplerian velocity channel. HCN,  $\text{H}^{13}\text{CN}$ , and  $\text{HC}^{15}\text{N}$  are shown from top to bottom. The Keplerian channels are those of Fig. B.1.

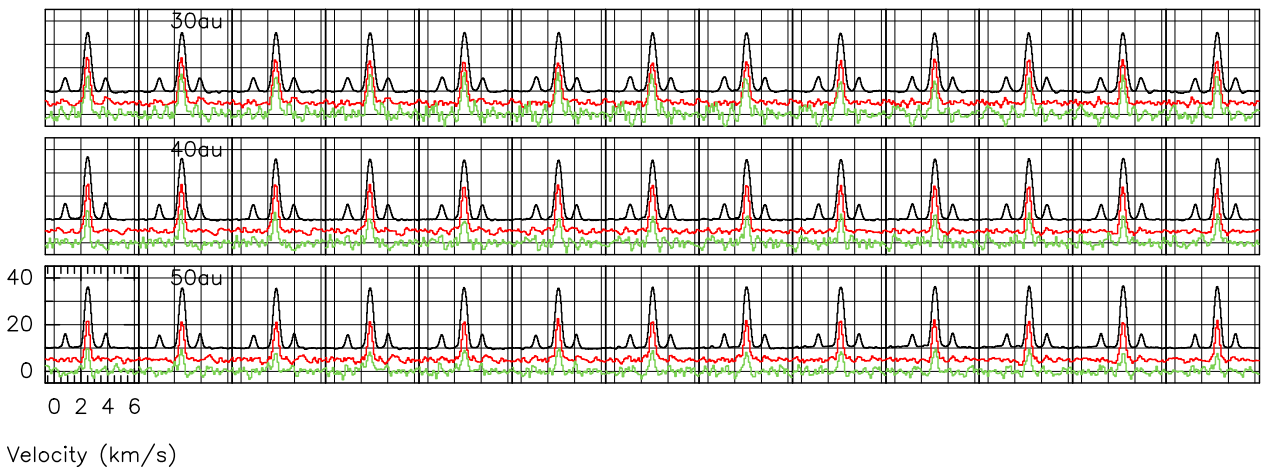


**Fig. B.3.** Spectra of HCN (black),  $\text{H}^{13}\text{CN}$  (red,  $\times 5$ ), and  $\text{HC}^{15}\text{N}$  (green,  $\times 10$ ) averaged within each Keplerian velocity channel (see e.g. Table B.1) and within annuli of constant thickness 5 au, centered at 30, 40, and 50 au (from top to bottom). The specific intensity scale is K using  $K/(\text{Jy/beam})$  conversion factors of 178.7, 188.1, and 189.0 for HCN,  $\text{H}^{13}\text{CN}$ , and  $\text{HC}^{15}\text{N}$ , respectively. The spectra have been shifted vertically for the sake of legibility.



**Table B.1.** Results of the Gaussian fits to the spatially averaged spectra of Fig. B.2.

$\nu_K - \nu_0^{\S}$	HCN <sup>a</sup>		H <sup>13</sup> CN <sup>b</sup>		HC <sup>15</sup> N <sup>c</sup>	
	$W^{\S}$	$\nu^{\S}$	$W^{\S}$	$\nu^{\S}$	$W^{\S}$	$\nu^{\S}$
-0.32	779.2(12.0)	2.515(1)	9.8(1)	2.494(3)	3.3(1)	2.491(5)
-0.26	803.2(13.1)	2.568(1)	9.8(2)	2.541(3)	3.6(1)	2.536(7)
-0.21	835.1(13.9)	2.634(1)	9.6(2)	2.612(4)	3.7(2)	2.611(10)
-0.16	871.0(12.7)	2.707(1)	10.1(2)	2.698(3)	3.7(2)	2.711(11)
-0.10	884.6(12.2)	2.753(1)	10.6(2)	2.746(4)	4.1(2)	2.756(10)
-0.05	892.4(13.7)	2.799(1)	10.9(2)	2.788(5)	4.5(2)	2.784(11)
0.00	850.0(14.2)	2.856(1)	10.4(2)	2.834(4)	4.6(2)	2.806(11)
0.05	838.8(14.1)	2.899(1)	10.0(2)	2.877(4)	4.5(2)	2.840(12)
0.11	847.7(14.7)	2.956(1)	9.7(2)	2.937(4)	3.9(2)	2.921(12)
0.16	870.9(16.9)	3.010(1)	9.6(2)	2.988(4)	3.6(2)	2.990(10)
0.21	881.2(16.1)	3.067(1)	9.6(2)	3.035(3)	3.5(2)	3.048(9)
0.27	870.2(15.5)	3.117(1)	9.6(2)	3.080(4)	3.5(2)	3.113(10)
0.32	859.7(14.2)	3.166(1)	9.8(2)	3.138(3)	3.7(2)	3.165(11)

NOTE.—Statistical uncertainties (at the  $1\sigma$  level) are written in brackets in units of the last digit.

<sup>§</sup> Keplerian minus systemic velocity ( $\text{km s}^{-1}$ ),  $W$  is the integrated flux in  $\text{mJy/beam km s}^{-1}$ , and  $\nu$  the central velocity in  $\text{km s}^{-1}$ .

<sup>a</sup> For HCN, the integrated intensity is computed as the total flux of the two weak lines divided by the sum of their relative intensities, 4.2%, while the center velocity is that of the main, central, component.

<sup>b,c</sup> The hf lines are not separated and a single Gaussian was fitted to the the main line.

**Table B.2.** Isotopic ratios from the spatially averaged spectra.

$\nu_K - \nu_0^{\S}$	$W_{12}^{\dagger}$		$W_{13}^{\dagger}$		$W_{15}^{\dagger}$		HCN/H <sup>13</sup> CN <sup>‡</sup>		HCN/HC <sup>15</sup> N <sup>‡</sup>		H <sup>13</sup> CN/HC <sup>15</sup> N <sup>‡</sup>	
-0.32	779.2	12.0	9.8	0.1	3.3	0.1	79.5	1.5	236.1	8.0	2.97	0.09
-0.26	803.2	13.1	9.8	0.2	3.6	0.1	82.0	2.1	223.1	7.2	2.72	0.09
-0.21	835.1	13.9	9.6	0.2	3.7	0.2	87.0	2.3	225.7	12.8	2.59	0.15
-0.16	871.0	12.7	10.1	0.2	3.7	0.2	86.2	2.1	235.4	13.2	2.73	0.16
-0.10	884.6	12.2	10.6	0.2	4.1	0.2	83.5	2.0	215.8	10.9	2.59	0.14
-0.05	892.4	13.7	10.9	0.2	4.5	0.2	81.9	2.0	198.3	9.3	2.42	0.12
0.00	850.0	14.2	10.4	0.2	4.6	0.2	81.7	2.1	184.8	8.6	2.26	0.11
0.05	838.8	14.1	10.0	0.2	4.5	0.2	83.9	2.2	186.4	8.9	2.22	0.11
0.10	847.7	14.7	9.7	0.2	3.9	0.2	87.4	2.4	217.4	11.8	2.49	0.14
0.16	870.9	16.9	9.6	0.2	3.6	0.2	90.7	2.6	241.9	14.2	2.67	0.16
0.21	881.2	16.1	9.6	0.2	3.5	0.2	91.8	2.5	251.8	15.1	2.74	0.17
0.27	870.2	15.5	9.6	0.2	3.5	0.2	90.6	2.5	248.6	14.9	2.74	0.17
0.32	859.7	14.2	9.8	0.2	3.7	0.2	87.7	2.3	232.4	13.1	2.65	0.15

NOTE.—<sup>§</sup>: Keplerian minus systemic velocity ( $\text{km s}^{-1}$ ) is that of the hf line of HCN at 354507.455 MHz. <sup>†</sup>:  $W_{12}$ ,  $W_{13}$ , and  $W_{15}$  are the integrated fluxes ( $\text{mJy/beam km s}^{-1}$ ) derived from Gaussian fitting (see also Table B.1). <sup>‡</sup>: integrated line flux ratios  $W_{12}/W_{13}$ ,  $W_{12}/W_{15}$ , and  $W_{13}/W_{15}$ . All uncertainties are statistical and at the  $1\sigma$  level.

of H<sub>2</sub> density ( $10^6$  to  $10^{11}$   $\text{cm}^{-3}$ ) and kinetic temperature (from 5 to 30 K) relevant to the TW Hya orbiting disk. The results of these calculations, in terms of  $T_{\text{ex}}$  are shown in Fig. C.1. As can be seen, there are significant departures at densities between  $10^6$   $\text{cm}^{-3}$  and  $10^8$   $\text{cm}^{-3}$ . At larger density, all lines are thermalized (models at  $n_{\text{H}_2}$  higher than  $10^9$   $\text{cm}^{-3}$  are not shown). From the generic chemical models of Visser et al. (2018), it appears that HCN is concentrated at radii  $r = 5 - 50$  au and scale heights  $z/r = 0.2$  to  $0.3$ , where the gas kinetic temperature is  $\approx 200$  K and the density in the range  $10^6$  to  $10^8$   $\text{cm}^{-3}$ , which would indicate that the single excitation temperature assumption fails.

On the other hand, the FWHM of the HCN, H<sup>13</sup>CN, and HC<sup>15</sup>N lines, at a radius of  $0.6''$  ( $\approx 35$  au) and beyond, is  $\approx 0.35$   $\text{km s}^{-1}$  (see Table B.3), placing a conservative upper limit on the kinetic temperature of (Teague et al. 2016)

$$(FWHM/2.35)^2 \times \mu m_{\text{H}} / (2k_B) \approx 35 \text{ K.} \quad (\text{C.1})$$

Referring to the tailored TW Hya model of van't Hoff et al. (2017), this upper limit, applied to the relevant range of radii, indicates that the density is larger than  $10^9$   $\text{cm}^{-3}$ , in a regime where lines should be thermalized, thus validating our single excitation temperature assumption. Our upper limit on the kinetic temperature is also well below the gas temperature of  $\sim 200$  K where the HCN abundance is the highest in the models of Visser et al. (2018), although we note that these models are generic ones and are not tailored to TW Hya.

**Table B.3.** Radial dependence of the line width (FWHM, km s<sup>-1</sup>) of HCN, H<sup>13</sup>CN, and HC<sup>15</sup>N.

$r$ (")	HCN	H <sup>13</sup> CN	HC <sup>15</sup> N
0.3	0.954±0.183	0.832±0.101	1.231±0.140
0.4	0.614±0.060	0.603±0.038	0.687±0.043
0.5	0.461±0.020	0.458±0.034	0.479±0.071
0.6	0.389±0.018	0.382±0.020	0.355±0.036
0.7	0.370±0.013	0.369±0.020	0.316±0.048
0.8	0.354±0.014	0.371±0.016	0.334±0.053
0.9	0.345±0.016	0.367±0.030	0.354±0.058

NOTE.—Spectra were averaged in annuli of thickness 0.1".  $r$  is the outer radius of each annulus.

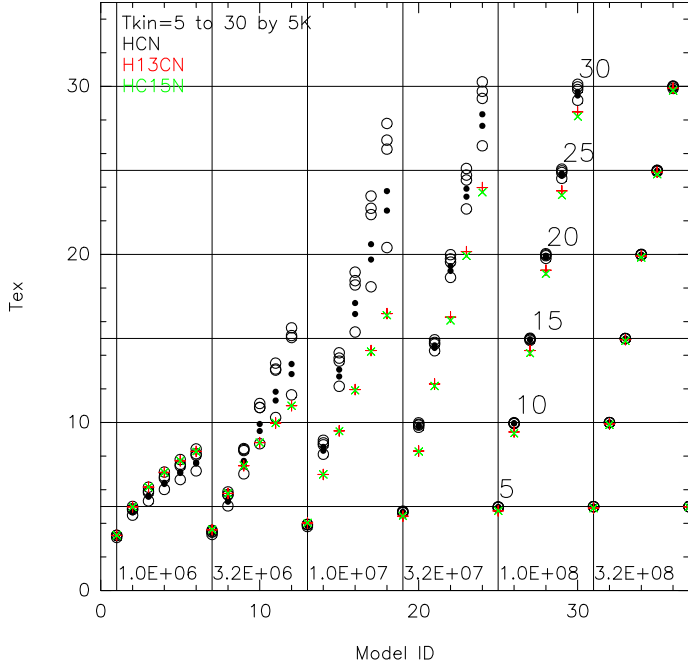


**Fig. C.1.** Excitation temperature of the 6 hf lines of HCN (see Table A.1) and the strongest hf lines of H<sup>13</sup>CN (red) and HC<sup>15</sup>N (green). The 4 overlapping hf lines of HCN are shown as open circles) and the two weakest, resolved, lines with filled dots.